

Nonlinear dynamic behavior of microscopic bubbles near a rigid wallSergey A. Suslov,¹ Andrew Ooi,² and Richard Manasseh³¹*Mathematics, H38, Swinburne University of Technology, Hawthorn, Victoria 3122, Australia*²*Department of Mechanical Engineering, University of Melbourne, Melbourne, Victoria 3010, Australia*³*Mechanical Engineering, H38, Swinburne University of Technology, Hawthorn, Victoria 3122, Australia*

(Received 20 February 2012; published 12 June 2012)

The nonlinear dynamic behavior of microscopic bubbles near a rigid wall is investigated. Oscillations are driven by the ultrasonic pressure field that arises in various biomedical applications such as ultrasound imaging or targeted drug delivery. It is known that, when bubbles approach a blood-vessel wall, their linear dynamic response is modified. This modification may be very useful for real-time detection of bubbles that have found targets; in future therapeutic technologies, it may be useful for controlled release of medical agents encapsulating microbubbles. In this paper, the nonlinear response of microbubbles near a wall is studied. The Keller-Miksis-Parlitz equation is adopted, but modified to account for the presence of a rigid wall. This base model describes the time evolution of the bubble surface, which is assumed to remain spherical, and accounts for the effect of acoustic radiation losses owing to liquid compressibility in the momentum conservation. Two situations are considered: the base case of an isolated bubble in an unbounded medium, and a bubble near a rigid wall. In the latter case, the wall influence is modeled by including a symmetrically oscillating image bubble. The bubble dynamics is traced using a numerical solution of the model equation. Subsequently, Floquet theory is used to accurately detect the bifurcation point where bubble oscillations stop following the driving ultrasound frequency and undergo period-changing bifurcations. Of particular interest is the detection of the subcritical period-tripling and -quadrupling transition. The parametric bifurcation maps are obtained as functions of nondimensional parameters representing the bubble radius, the frequency and pressure amplitude of the driving ultrasound field, and the distance from the wall. It is shown that the presence of the wall generally stabilises the bubble dynamics, so that much larger values of the pressure amplitude are needed to generate nonlinear responses. Thus, a clinical protocol in which selected nonlinear harmonics are examined under varying insonation amplitudes may be useful in detecting microbubble proximity to walls.

DOI: [10.1103/PhysRevE.85.066309](https://doi.org/10.1103/PhysRevE.85.066309)

PACS number(s): 47.55.dd, 43.25.Ts, 43.25.Yw, 43.80.Qf

I. INTRODUCTION

When driven by the ultrasound pressure field, microbubbles strongly scatter the incident acoustic waves and can resonate or fragment [1,2]. Owing to this property, intravenously injected microbubbles are actively used in clinical practice [3]. Their acoustic response makes the blood that transports them stand out in the scan relative to the surrounding tissue: this is “contrast” to the clinician. Modern microbubble contrast agents are coated with an elastic shell to retard their dissolution [4,5] and to modify their properties [1,6]. For example, the microbubble shells can contain molecules such as antibodies that adhere to specific disease markers [7]. However, despite significant research into the nature of the signal of target-bound microbubbles [8–10], antibody-coated microbubbles are not in clinical use since at present there is no clinically accepted way to tell adherent microbubbles from free ones in real time [11–13]. Thus, developing a method for a rapid discrimination of bubbles during their short lifetime would be an important step toward clinical practice [10]. Suggestions so far have included filtering based on the fact that the speed of adherent microbubbles should be zero [12,13]. However, this does not discriminate reliably between microbubbles trapped in the blood-vessel boundary layer and ones truly adhered. Alternatively, it was suggested to “push” microbubbles with the acoustic radiation force so that only the free microbubbles would move, thus enabling the difference from bound microbubbles to be discerned [14]. A further suggestion was to exploit alterations in the linear response frequency [15] that characterize adherent bubbles.

If viscous forces acting in the fluid near the wall are neglected, potential-flow theory allows the wall to be replaced with an identical “mirror” bubble image that is located symmetrically with respect to the rigid wall (see Fig. 1) and oscillates with the same frequency, amplitude, and phase as the original bubble [16]. This mirror-pair oscillates in the symmetric coupled-bubble mode [17,18]. Previous studies of such a configuration showed that the linear natural frequency of the bubble near the wall is shifted downward by a factor of $\sqrt{2/3} \approx 0.82$ [16,18]. It was found to be numerically consistent with the predicted values, although for bubbles that were somewhat larger than typical contrast-agent bubbles [15]. Recent experiments with high-speed imaging also demonstrated a downshift in the linear response frequency of actual contrast agents on biological target surfaces [19].

While some progress has been achieved in this area of research, most of the results so far were obtained for monodispersed bubbles [20,21]. However, in realistic clinical applications bubbles vary greatly in size and thus resonant frequency. Thus adding further indicators of proximity to target walls to the techniques already suggested in the literature (see, e.g., [22,23]) is vital for improving the sensitivity and specificity of microbubble targeting.

Detailed research into the nonlinear dynamics of a single, isolated microbubble began with the work of Lauterborn in 1976 [24] and by 1990 detailed bifurcation diagrams were calculated illustrating the complex behavior possible as driving frequency and amplitude were changed [25]. Recently, the

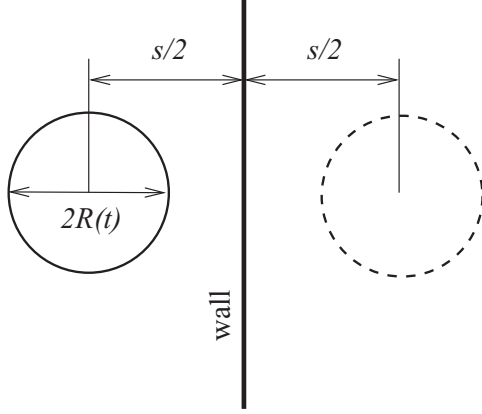


FIG. 1. Schematic view of the problem geometry.

effect of acoustic coupling with neighboring bubbles was examined numerically in Ref. [26] using a coupled-oscillator approach. In the present paper, we expand on the earlier suggestions for detection of microbubbles on walls based on linear theory to a study of the nonlinear dynamics of a microbubble in the vicinity of a solid wall. In particular, we discuss the nonuniqueness of nonlinear bubble oscillations that occur for the same driving parameters but different initial conditions.

In addition to the neglect of viscosity inherent in the mirror-image theory, we also assume that the distance $s/2$ between the wall and the bubble center remains constant (in reality, Bjerknes forces would cause this distance to vary [27,28]). The effects of the bubble shell, which differ widely among microbubble types (and differ among models of the shell) [29,30], are also neglected. Besides, in the medical application that motivated the present work, the walls of blood vessels are unlikely to be rigid as is assumed here and there is an indication that the elasticity of the wall may have a noticeable contribution to the acoustic signature of the bubbles oscillating in its vicinity [31]. Such influences are also not accounted for in the current study.

The above assumptions are made to simplify the calculations. They will be refined in the future. For the present, the immediate aim is simply to determine if potentially useful differences exist in the nonlinear dynamics between adherent and free microbubbles. As noted earlier, the ultimate aim is to derive further criteria of wall proximity.

II. MODIFIED KELLER-MIKSIS-PARLITZ EQUATION

The base model employed in the current study is the Keller-Miksis-Parlitz [25,32] equation modified to account for the presence of an image bubble imitating the interaction of a physical bubble with a rigid wall [33] [see the last term in the right-hand side of equation (1)],

$$\begin{aligned} & \left(1 - \frac{\dot{R}}{c}\right) R \ddot{R} + \frac{\dot{R}^2}{2} \left(3 - \frac{\dot{R}}{c}\right) \\ &= \frac{1}{\rho} \left[1 + \frac{\dot{R}}{c} + \frac{R}{c} \frac{d}{dt}\right] [P(R, \dot{R}) \\ & \quad - P_\infty(t)] - \frac{1}{s} (R^2 \ddot{R} + 2R \dot{R}^2), \end{aligned} \quad (1)$$

where

$$P(R, \dot{R}) = \left(P_0 - P_v + \frac{2\sigma}{R_0}\right) \left(\frac{R_0}{R}\right)^{3\kappa} - \frac{4\mu\dot{R}}{R} - \frac{2\sigma}{R}. \quad (2)$$

The expression $P_\infty(t) = P_0 - P_v + \alpha \sin(\omega t)$, where $\omega = 2\pi f_e$, represents the pressure in the liquid far from the bubble, and $R(t)$, R_0 , μ , ρ , κ , c , σ , α , and f_e denote the instantaneous bubble radius, the equilibrium bubble radius, the dynamic viscosity of the liquid, the density of the liquid, the polytropic exponent of a gas entrapped in the bubble, the speed of sound in the liquid, the surface tension of a gas-liquid interface, the acoustic pressure amplitude, and the driving frequency, respectively. The model considered accounts for the decay of bubble oscillations due to viscous dissipation and acoustic radiation. Acoustic radiation losses are represented by terms involving the (finite) speed of sound c in the Keller-Miksis-Parlitz equation. Bubble oscillations can also decay due to thermal energy losses, but such damping is neglected in comparison with viscous effects [34]. While the speed of sound is finite in the model employed here it is assumed to be sufficiently large so that the phase variation in the incoming ultrasound field over the distances of the order of the bubble radius are neglected. Despite various simplifying assumptions used in the derivation of Keller-Miksis-Parlitz equation the comparison of its numerical solutions with experimental observations of bubbles oscillating in the vicinity of a rigid wall has demonstrated a reasonable agreement [18,35].

In many bubble-acoustic studies, equations are left in dimensional form. However, to reduce the total number of the governing parameters, we make equation (1) nondimensional by using the equilibrium radius R_0 and the inverse ultrasound frequency ω^{-1} as the length and time scales, respectively, so that the equation is rewritten in terms of the nondimensional bubble radius $r = R(t)/R_0$ and time $\tau = \omega t$ as

$$\begin{aligned} & \ddot{r} [(1 - \Omega \dot{r})r + \Omega \mathcal{R} + \mathcal{S}r^2] \\ &= (\Omega \dot{r} - 3) \frac{\dot{r}^2}{2} - \frac{\mathcal{W} + \mathcal{R}\dot{r}}{r} + (\mathcal{M} + \mathcal{W}) \frac{[1 + (1 - 3\kappa)\Omega \dot{r}]}{r^{3\kappa}} \\ & \quad - (1 + \Omega \dot{r})(\mathcal{M} + \mathcal{M}_e \sin \tau) - \mathcal{M}_e \Omega r \cos \tau - 2\mathcal{S}r\dot{r}^2, \end{aligned} \quad (3)$$

where

$$\begin{aligned} \Omega &= \frac{\omega R_0}{c}, \quad \mathcal{R} = \frac{4\mu}{\rho \omega R_0^2}, \quad \mathcal{W} = \frac{2\sigma}{\rho \omega^2 R_0^3}, \\ \mathcal{M} &= \frac{P_0 - P_v}{\rho \omega^2 R_0^2}, \quad \mathcal{M}_e = \frac{\alpha}{\rho \omega^2 R_0^2}, \quad \mathcal{S} = \frac{R_0}{s}. \end{aligned} \quad (4)$$

Each of the nondimensional groups listed above has a straightforward physical meaning. Since in practical applications the driving ultrasound frequency is usually fixed, parameter Ω , which is the ratio of the equilibrium bubble radius and the acoustic wavelength, characterizes the bubble size. Parameters \mathcal{R} and \mathcal{W} characterize the viscous dissipation and surface tension effects, respectively. They can be treated as inverse Reynolds and Weber numbers.

Parameter \mathcal{M} represents elastic properties of the gas and its compressibility, while \mathcal{M}_e is the measure of the external acoustic excitation. Finally, parameter \mathcal{S} is effectively the inverse distance between the bubble center and the wall.

III. RANGE OF PARAMETRIC VALUES OF INTEREST

Fluids where microbubble acoustics is of primary practical interest are typically water-based. Therefore, in order to estimate the values of the governing nondimensional parameters we use the following fluid properties corresponding to water at 20 °C: $c = 1484$ m/s, $\mu = 10^{-3}$ kg m/s, $\sigma = 7.25 \times 10^{-2}$ N/m, $\rho = 10^3$ kg/m³, $p_v = 2330$ Pa. We also assume that the gas trapped inside the bubble is air at atmospheric pressure $P_0 = 10^5$ Pa and use the value of $\kappa = \frac{4}{3}$ for the polytropic exponent.

A typical practical range of the microbubble radii is $R_0 = 0.5 - 20$ μm . The frequency used in medical ultrasound imaging is around $f_e = 1$ MHz, and the driving pressure amplitude is in the range $\alpha = 10^5 - 10^6$ Pa. In this study we consider bubbles that are assumed to preserve their spherical shape. This introduces the natural limitation on the value of $s > 2R_0$. For these physical parameters the values of nondimensional groups \mathcal{M} , \mathcal{W} , \mathcal{R} and Ω estimated for bubbles of various radii are linked as

$$\mathcal{R} = \frac{\mathcal{R}_0}{\Omega^2}, \quad \mathcal{W} = \frac{\mathcal{W}_0}{\Omega^3}, \quad \mathcal{M} = \frac{\mathcal{M}_0}{\Omega^2}, \quad \mathcal{M}_e = \frac{\mathcal{M}_{e0}}{\Omega^2}, \quad (5)$$

where

$$\begin{aligned} \mathcal{R}_0 &= \frac{4\mu\omega}{\rho c^2} \approx 1.14 \times 10^{-5}, \\ \mathcal{W}_0 &= \frac{2\sigma\omega}{\rho c^3} \approx 2.79 \times 10^{-7}, \\ \mathcal{M}_0 &= \frac{P_0 - P_v}{\rho c^2} \approx 4.43 \times 10^{-5}, \\ 4.5 \times 10^{-5} &\lesssim \mathcal{M}_{e0} = \frac{\alpha}{\rho c^2} \lesssim 4.5 \times 10^{-4}, \end{aligned} \quad (6)$$

for $0.002 \lesssim \Omega \lesssim 0.085$ (see Fig. 2), and $10^5 \text{ Pa} < \alpha < 10^6 \text{ Pa}$. For $\Omega \gtrsim 0.008$ corresponding to $R_0 \gtrsim 2$ μm the magnitude of \mathcal{M} exceeds those of \mathcal{W} and \mathcal{R} ; see Fig. 2(b). This represents the well-known fact that the dynamics of larger microbubbles is mostly determined by the gas elasticity, while both viscous dissipation and surface tension play secondary roles. However, for smaller bubbles the value of \mathcal{W} increases rapidly [i.e., cubically; see (5)] and thus bubble dynamics is influenced by the surface tension to a greater degree. The role of viscosity for microbubbles of all sizes remains relatively small.

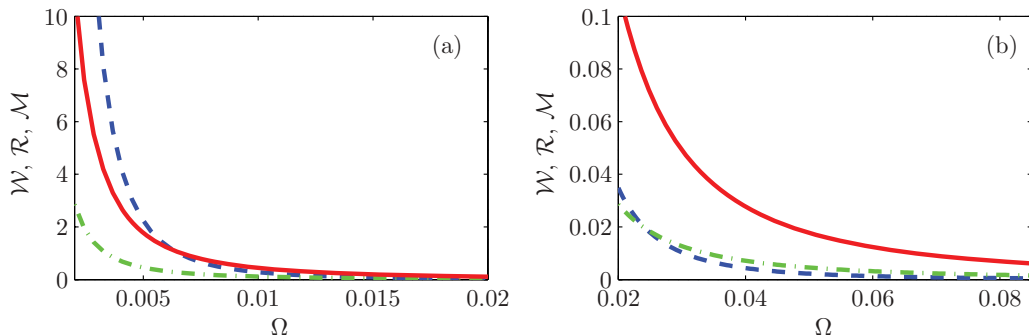


FIG. 2. (Color online) Variation of nondimensional parameters \mathcal{W} (dash-dotted line), \mathcal{R} (dashed line), and \mathcal{M} (solid line) with the nondimensional bubble radius Ω : (a) $\Omega < 0.02$, (b) $\Omega > 0.02$.

The other two independent nondimensional parameters are \mathcal{S} and \mathcal{M}_e . The value of \mathcal{S} varies from 0 (isolated bubble far away from the wall) to 1/2 (bubble near the wall), while typical values of \mathcal{M}_e range from 0 to around 0.4 for bubbles greater than about 5 μm , but can be of order 10 for bubbles smaller than 2 μm in diameter.

IV. SMALL AMPLITUDE OSCILLATIONS

When the nondimensional driving ultrasound pressure amplitude \mathcal{M}_e is small, the bubble oscillates near its equilibrium state so that its instantaneous nondimensional radius is $r(t) = 1 + r_1(t)$, where $r_1(t) \ll 1$. Linearizing equation (3) about $r = 1$ we obtain

$$\begin{aligned} (1 + \Omega\mathcal{R} + \mathcal{S})\ddot{r}_1 + (\mathcal{R} + \Omega\mathcal{A})\dot{r}_1 + \mathcal{A}r_1 \\ = -\mathcal{M}_e(\Omega \cos \tau + \sin \tau) = -\mathcal{M}_e\sqrt{1 + \Omega^2} \sin(\tau + \phi), \end{aligned} \quad (7)$$

where $\mathcal{A} \equiv (3\kappa - 1)\mathcal{W} + 3\kappa\mathcal{M}$ and $\phi = \tan^{-1} \Omega$. The solution of this linear equation is

$$r_1(t) = e^{-\frac{t}{\tau_0}} (a \sin \omega_0 t + b \cos \omega_0 t) + a_0 \sin(\tau + \phi_0) \quad (8)$$

if $D = (\mathcal{R} - \Omega\mathcal{A})^2 - 4(1 + \mathcal{S})\mathcal{A} < 0$ (this condition is always satisfied if the viscosity of the fluid remains small as is the case in the problem considered). It suggests that the characteristic relaxation time τ_0 over which the magnitude of the transient solution reduces by the factor of e , the natural frequency ω_0 of bubble oscillations, the amplitude a_0 and the phase shift $\phi_0 - \phi$ of the forced small amplitude bubble oscillations are given by

$$\tau_0 = 2 \frac{1 + \Omega\mathcal{R} + \mathcal{S}}{\mathcal{R} + \Omega\mathcal{A}} \approx 2 \frac{1 + \mathcal{S}}{\mathcal{R}_0} \Omega^2, \quad (9)$$

$$\omega_0 = \frac{\sqrt{-D}}{2(1 + \Omega\mathcal{R} + \mathcal{S})} \approx \sqrt{\frac{\mathcal{A}}{1 + \mathcal{S}}}, \quad (10)$$

$$\begin{aligned} a_0 &= \mathcal{M}_e \sqrt{\frac{1 + \Omega^2}{(1 + \Omega\mathcal{R} + \mathcal{S} - \mathcal{A})^2 + (\mathcal{R} + \Omega\mathcal{A})^2}} \\ &\approx \frac{\mathcal{M}_e}{|1 + \mathcal{S} - \mathcal{A}|}, \end{aligned} \quad (11)$$

$$\phi_0 - \phi = \tan^{-1} \frac{\mathcal{R} + \Omega\mathcal{A}}{1 + \Omega\mathcal{R} + \mathcal{S} - \mathcal{A}} \approx \tan^{-1} \frac{\mathcal{R}_0}{(1 + \mathcal{S} - \mathcal{A})\Omega^2}, \quad (12)$$

where

$$\mathcal{A} \approx \begin{cases} (3\kappa - 1) \frac{W_0}{\Omega^3}, & \Omega \ll \Omega_0 \\ 3\kappa \frac{M_0}{\Omega^2}, & \Omega \gg \Omega_0, \end{cases} \quad (13)$$

$$\Omega_0 = \frac{3\kappa - 1}{3\kappa} \frac{\mathcal{W}_0}{\mathcal{M}_0} \approx 0.0047.$$

The approximate values above are obtained by retaining only the largest parameters [see Fig. 2 and equations (5) and (7)] entering the expressions. These formulas provide a straightforward means of identifying the dominant physical processes taking place in acoustically forced microbubble oscillations. The value of Ω_0 determines the bubble size at which the major physical property determining the characteristics of bubble oscillations switches from surface tension of the gas-liquid interface to elasticity of the entrapped gas. As noted earlier, and now quantified by (13), for the considered fluid properties, only very small bubbles with radii smaller than about $1 \mu\text{m}$ would be affected by the surface tension. We also conclude that the bubble oscillation energy dissipation rate increases and, subsequently, the relaxation time decreases due to the action of two physical mechanisms: a viscous dissipation characterized by \mathcal{R} and losses due to the acoustic radiation of the bubble, which are proportional to $\kappa\Omega\mathcal{M}$, yet viscous dissipation always dominates the relaxation process. The proximity of the wall (e.g., the increasing value of \mathcal{S}) leads to an increase in the relaxation time; that is, to the preservation of the oscillation energy due to the reflection of acoustic waves from the wall back toward the bubble. This decrease in damping owing to

the presence of the wall under linear theory has been noted before [16,36].

As mentioned in Sec. III, the natural frequency of small-amplitude bubble oscillations at $\Omega > \Omega_0$ (this condition is satisfied for almost a complete range of bubble sizes used in practice) is predominantly determined by the gas elasticity with the surface tension playing a negligible role. The amplitude of oscillations is directly proportional to that of the ultrasound forcing \mathcal{M}_e and decreases due to the restricting influence of the wall as \mathcal{S} increases (when the bubble approaches the wall). The phase lag $\phi_0 - \phi$ between the forcing and the bubble response is mostly due to the effects of fluid viscosity and acoustic radiation. The proximity of the wall forces a bubble to follow the external excitation more closely.

The variations of characteristics of small-amplitude oscillations with the nondimensional bubble radius are presented in Fig. 3. The overall trends are that the relaxation time increases and the natural frequency of bubble oscillations decreases with bubble radius. From a computational point of view it is important to note that, depending on the initial conditions and the bubble equilibrium size, it could be required to integrate the governing equations over more than 300 forcing periods before a statistically steady solution can be established for a bubble located away from the wall. For a near-wall bubble the transient time can be greater by at least a factor of two.

One of the most important sources of information regarding the anticipated bubble behavior is the bubble natural frequency diagram shown in Fig. 3(b). The value of ω_0 monotonically decreases with the nondimensional bubble radius Ω and

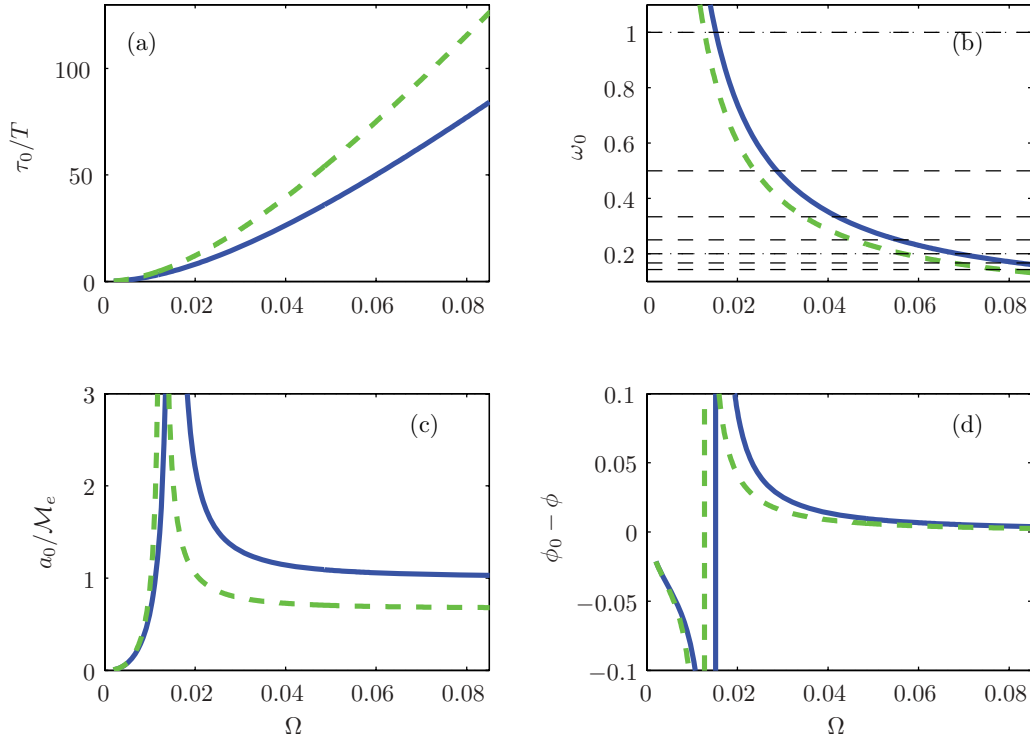


FIG. 3. (Color online) Characteristics of small amplitude oscillations as functions of the nondimensional bubble radius Ω for a bubble away from ($\mathcal{S} = 0$, solid lines) and near the wall ($\mathcal{S} = \frac{1}{2}$, dashed lines). Intersections of the horizontal dashed lines with the ω_0 lines in plot (b) correspond to subharmonic resonance values of Ω listed in Table I.

TABLE I. Values of parameter Ω at which subharmonic resonances with frequencies listed in the top row are expected to occur for a bubble away (middle row) and near the wall (bottom row).

ω_0	1	$\frac{1}{2}$	$\frac{1}{3}$	$\frac{1}{4}$	$\frac{1}{5}$	$\frac{1}{6}$	$\frac{1}{7}$
$\Omega (\mathcal{S} = 0)$	0.0152	0.0287	0.0421	0.0554	0.0688	0.0821	0.0955
$\Omega (\mathcal{S} = \frac{1}{2})$	0.0128	0.0238	0.0348	0.0456	0.0566	0.0674	0.0784

becomes unity at

$$\Omega = \Omega_1 \approx \sqrt{\frac{3\kappa\mathcal{M}_0}{1+\mathcal{S}}} \quad (14)$$

(see Table I for numerical values), which corresponds to the size of the bubble at which it resonates strongly with the external forcing. Typical resonance features such as a rapid increase of the bubble oscillation amplitude up to the maximum value

$$a_{0\max} \approx \frac{\Omega_1^2 \mathcal{M}_e}{\mathcal{R}_0} = \frac{3\kappa\mathcal{M}_0\mathcal{M}_e}{(1+\mathcal{S})\mathcal{R}_0} \quad (15)$$

and the switch of the phase lag $\phi_0 - \phi$ from $\frac{\pi}{2}$ to $-\frac{\pi}{2}$ are observed at this point; see Figs. 3(c) and 3(d). For $\Omega < \Omega_1$ the amplitude of bubble oscillations decreases very rapidly [see Fig. 3(c)]. A bubble effectively stops responding to an incoming ultrasound wave and becomes “invisible” in acoustic imaging applications. Therefore, in our further analysis we focus on the nontrivial bubble behavior observed at $\Omega > \Omega_1$. We also note that the small amplitude oscillations of a bubble near the wall are similar to those of a distant bubble, however the resonance shifts toward smaller values of Ω_1 (see Table I). This frequency shift has been also noted in Ref. [18] and the potential value of a frequency shift in identifying targeted microbubbles via a filtering approach has been recognized in Ref. [15]. Therefore, it is expected that the acoustic signature of initially “silent” small bubbles will become more pronounced as they approach the wall. This feature can potentially be used for estimating the likelihood of bubbles reaching the walls of blood vessels in applications such as targeted drug delivery and ultrasound imaging.

The fact that the nondimensional natural frequency of bubble oscillations remains smaller than 1 for a large portion of the practical bubble size range suggests that nonlinear subharmonic resonances can occur. The intersections of the horizontal dashed lines with the ω_0 curves in Fig. 3(b) define the subharmonic resonant values of Ω which are listed in Table I. Of course, the subharmonic resonances can only exist owing to nonlinear effects manifested when the amplitude is no longer small. As will be shown in the subsequent sections, the presence of subharmonic resonances defines what type of oscillations are observed. Finally, we note that larger distant and near-wall bubbles follow the external forcing quite closely so that the phase lag remains close to zero away from the main resonance.

V. FINITE AMPLITUDE PERIODIC SOLUTIONS

A. Floquet analysis

When the forcing amplitude \mathcal{M}_e increases, the bubble oscillation amplitude becomes large and solutions discussed

in the previous section are replaced with nonlinear solutions $r_0(\tau)$. The solutions are not sinusoidal anymore, yet are still T periodic, where $T = 2\pi$ is the period of the external forcing. However, this remains true only up to a certain critical value of the forcing amplitude at which the T -periodic solution undergoes a bifurcation to a different state. To determine the exact parametric values for the bifurcation point and the nature of the bifurcation we look for a solution in the form $r(t) = r_0(\tau) + r'(\tau)$, where we assume that $r'(\tau) \ll r_0(\tau)$ over the period of one forced oscillation. Numerically, $r_0(\tau)$ is obtained by solving equation (3) with the periodic boundary conditions $r_0(0) = r_0(T)$ and $\dot{r}_0(0) = \dot{r}_0(T)$ (see Appendix for details of numerical implementation). To investigate the stability of such a solution we consider the linearization of equation (3) about $r_0(\tau)$

$$\begin{aligned} & [(1 - \Omega\dot{r}_0)r_0 + \Omega\mathcal{R} + \mathcal{S}r_0^2]\ddot{r}' \\ &= - \left[3\dot{r}_0 + \frac{\mathcal{R}}{r_0} + 4\mathcal{S}r_0\dot{r}_0 + \Omega \left(\mathcal{M} - \frac{3}{2}\dot{r}_0^2 - R_0\ddot{r}_0 \right. \right. \\ &\quad \left. \left. + \frac{(3\kappa - 1)(\mathcal{M} + \mathcal{W})}{r_0^{3\kappa}} + \mathcal{M}_e \sin t \right) \right] \dot{r}' \\ &+ \left[\frac{\mathcal{W} + r_0\dot{r}_0}{r_0^2} - (1 - \Omega\dot{r}_0)\ddot{r}_0 \right. \\ &\quad \left. - \frac{3\kappa(\mathcal{M} + \mathcal{W})[1 + (1 - 3\kappa)\Omega\dot{r}_0]}{r_0^{3\kappa+1}} \right] r' \\ &\quad - \mathcal{M}_e\Omega \cos t - 2\mathcal{S}(\dot{r}_0^2 + r_0\ddot{r}_0) \dot{r}', \end{aligned} \quad (16)$$

and apply Floquet analysis [37]. In brief, we solve equation (17) with known periodic coefficients depending on $r_0(\tau)$ and $\dot{r}_0(\tau)$ over the interval $\tau \in [0, T]$ subject to two sets of linearly independent initial conditions $[r'_1(0), \dot{r}'_1(0)] = [1, 0]$ and $[r'_2(0), \dot{r}'_2(0)] = [0, 1]$. The values of the obtained solutions at $\tau = T$ form a monodromy matrix Y

$$Y = \begin{bmatrix} r'_1(T) & r'_2(T) \\ \dot{r}'_1(T) & \dot{r}'_2(T) \end{bmatrix}, \quad (17)$$

whose (generally complex) eigenvalues $\sigma_{1,2} = \sigma_{1,2}^R + i\sigma_{1,2}^I = |\sigma_{1,2}|e^{i\theta_{1,2}}$ are Floquet multipliers. According to the Floquet theorem, the solution of equation (17) satisfies the following relationship:

$$[r'(nT), \dot{r}'(nT)] = \sigma^n [r'(0), \dot{r}'(0)] = |\sigma|^n e^{in\theta} [r'(0), \dot{r}'(0)]. \quad (18)$$

Therefore, the periodic solution $r_0(\tau)$ is unstable if the magnitude of at least one of the Floquet multipliers, $\max |\sigma_{1,2}|$, exceeds unity. At the bifurcation point we must have $\max |\sigma_{1,2}| = 1$. This condition determines neutral stability of a periodic solution with respect to infinitesimal disturbances and the bifurcation type is determined by the complex value of the Floquet multiplier with the unit magnitude. For example, if $\sigma = e^{2i\pi/n}$ so that $\sigma^n = \sigma^{2i\pi} = 1$ then the solution of Eq. (17) will be repeated for the first time after n forcing periods T :

$$\begin{aligned} r'(nT) &= r'(0), & \dot{r}'(nT) &= \dot{r}'(0), \\ r'(mT) &\neq r'(0), & \dot{r}'(mT) &\neq \dot{r}'(0), \end{aligned}$$

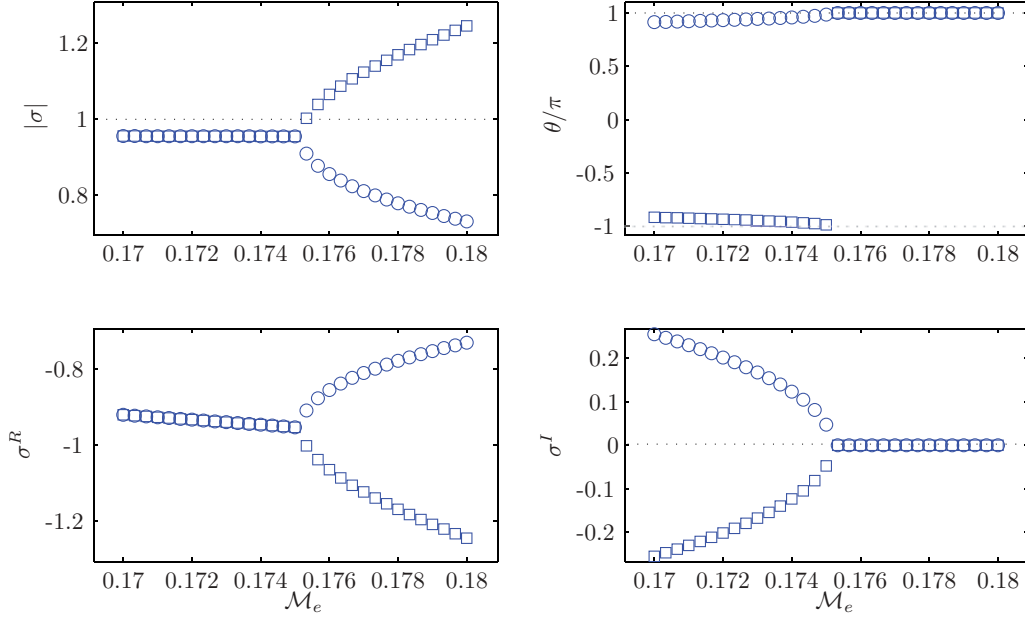


FIG. 4. (Color online) Floquet multipliers for medium amplitude bubble oscillations away from the wall ($S = 0$) at $\Omega = 0.0423$. Circles and squares correspond to two distinct multipliers.

where $m < n$, meaning that the $T \rightarrow nT$ bifurcation has occurred. In particular, in the situation when one of the Floquet multipliers becomes equal to $e^{i\pi} = -1$ (i.e., when $n = 2$), a period-doubling bifurcation is observed.

B. Medium amplitude oscillations

The typical behavior of Floquet multipliers as the forcing amplitude \mathcal{M}_e increases is illustrated in Fig. 4. The magnitude of one of the multipliers increases above the value of 1 while the second multiplier remains smaller than unity. The phase of the larger of the two Floquet multipliers becomes $\theta = \pi$ meaning that $n = 2\pi/\theta = 2$ and thus the period-doubling bifurcation occurs at $\mathcal{M}_e = \mathcal{M}_{e,cr}$. Note that a bifurcation of Floquet multipliers seen in Fig. 4 is not related to the period-doubling bifurcation of the solution of Eq. (3); the latter is determined only by the fact that one of the multipliers becomes equal to -1 regardless of whether σ itself undergoes any bifurcations. Thus the parametric location of a bifurcation point is accurately determined by Floquet multipliers that change continuously with \mathcal{M}_e with one of them becoming equal to -1 at the critical value of $\mathcal{M}_e = \mathcal{M}_{e,cr}$.

The period-doubling bifurcations are detected in small to medium amplitude oscillations for all considered values of nondimensional bubble radius Ω . Numerical experiments confirm that the transition between T - and $2T$ -periodic solutions occurs at the same value of $\mathcal{M}_e = \mathcal{M}_{e,cr}$ regardless of whether \mathcal{M}_e is gradually increased or decreased. Since no hysteresis is observed we conclude that microbubbles undergo supercritical period-doubling bifurcation in all considered regimes.

The examples of bubble oscillations for $\Omega = 0.0423$ corresponding to the equilibrium bubble radius $R_0 = 10 \mu\text{m}$ before and after the period-doubling bifurcations occurring at $\mathcal{M}_{e,cr} \approx 0.17532$ for a bubble away from the wall and at $\mathcal{M}_{e,cr} \approx 0.32621$ for a bubble near the wall are shown in Figs. 5 and 6. While the qualitative behavior of the distant and near-wall bubbles remains the same we note that the proximity of the wall causes a significant increase in the ultrasound pressure required to induce a supercritical period-doubling bifurcation. Equivalently, this means that the presence of the wall has a strong stabilizing influence on the oscillations of bubbles with the equilibrium radius $R_0 \gtrsim 10 \mu\text{m}$. The pressure amplitude that would have to be applied to cause period doubling is nearly doubled by proximity to the wall. In

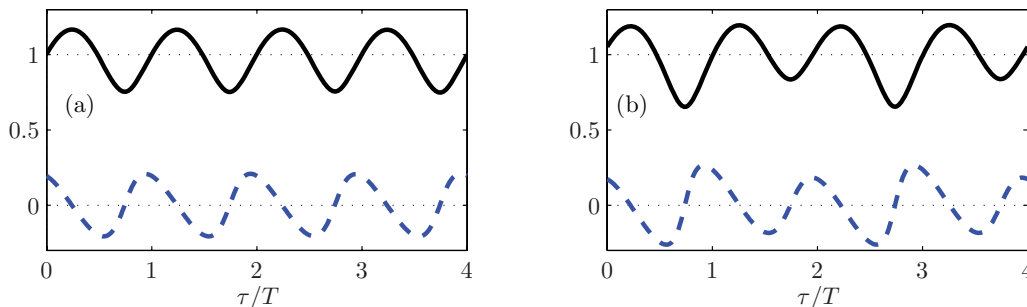


FIG. 5. (Color online) Bubble oscillations away from wall ($S = 0$) at $\Omega = 0.0423$ (a) before ($\mathcal{M}_e = 0.17$) and (b) after ($\mathcal{M}_e = 0.18$) period-doubling bifurcation. The solid and dashed lines represent $r(\tau)$ and $\dot{r}(\tau)$, respectively.

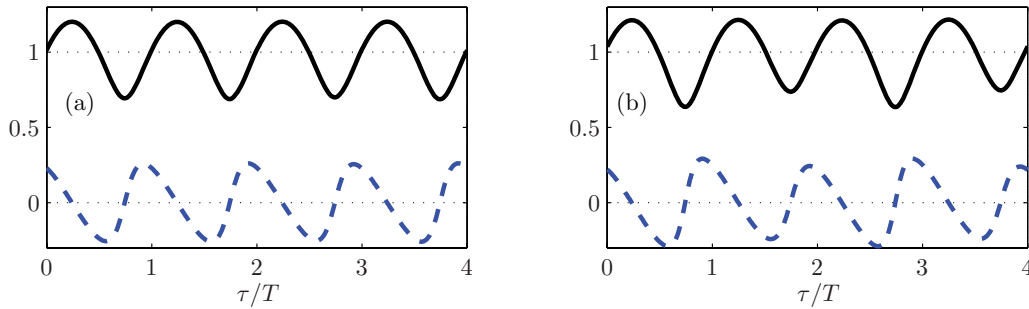


FIG. 6. (Color online) Oscillations of a bubble near wall ($S = \frac{1}{2}$) at $\Omega = 0.0423$ (a) before ($\mathcal{M}_e = 0.32$) and (b) after ($\mathcal{M}_e = 0.33$) period-doubling bifurcation. The solid and dashed lines represent $r(\tau)$ and $\dot{r}(\tau)$, respectively.

clinical terminology, this implies that an ultrasound scanner would have to be set to produce twice the “mechanical index” in order to see this nonlinear response at the wall; a very significant change. However, we will show in the following sections that, for smaller bubbles, this trend is reversed.

C. Large amplitude oscillations

Away from the parametric location of the period-doubling bifurcation, the magnitudes of Floquet multipliers computed for small amplitude T -periodic solutions [that are accurately approximated by (8)] for a bubble located far away from the wall remain smaller than unity; see Fig. 7. This means that such oscillations are stable and the bubble can follow external ultrasound excitation for an indefinitely long time [see Fig. 8(a)]. However, the phase θ of the Floquet multipliers provides very remarkable information. It turns out that $\theta_{1,2}$ asymptotes to the values $\pm 2\pi/3$. Thus $n = 2\pi/\theta_{1,2} = \pm 3$. Even though no bifurcation is detected, since $|\sigma_{1,2}| < 1$, the Floquet multipliers strongly indicate that a $3T$ -periodic solution may exist. However, in contrast to the $2T$ -periodic

solution, it is disjoint from the T -periodic solution in that sense that it cannot be obtained from it via a continuous variation of physical governing parameters such as Ω or \mathcal{M}_e alone.

A careful numerical investigation reveals that the governing equation (3) indeed admits large amplitude oscillation solutions that are not described by (8) even when the external forcing is weak. Consistent with the predictions based on Floquet analysis, such large amplitude oscillations have a larger period of $3T$ as is confirmed by Fig. 8(b). In particular, for the bubble of equilibrium radius $R_0 = 10 \mu\text{m}$ ($\Omega = 0.0423$), the minimum value of the forcing amplitude at which the $3T$ -periodic solution is still detected numerically is found to be $\mathcal{M}_e \approx 0.0342$ (corresponding to $\alpha \approx 135 \text{ kPa}$) which agrees well with the value estimated from Fig. 10(a) in Ref. [26].

Similarly, Floquet multipliers computed away from a period-doubling bifurcation for a bubble near the wall (see Fig. 9), confirm that small amplitude T -periodic solutions are stable; see Fig. 10(a). However, in contrast to the distant bubble case, the phase θ of Floquet multipliers asymptotes to the value of $\theta_{1,2} = \pm\pi/2$ so that $n = 2\pi/\theta = 4$ indicating the

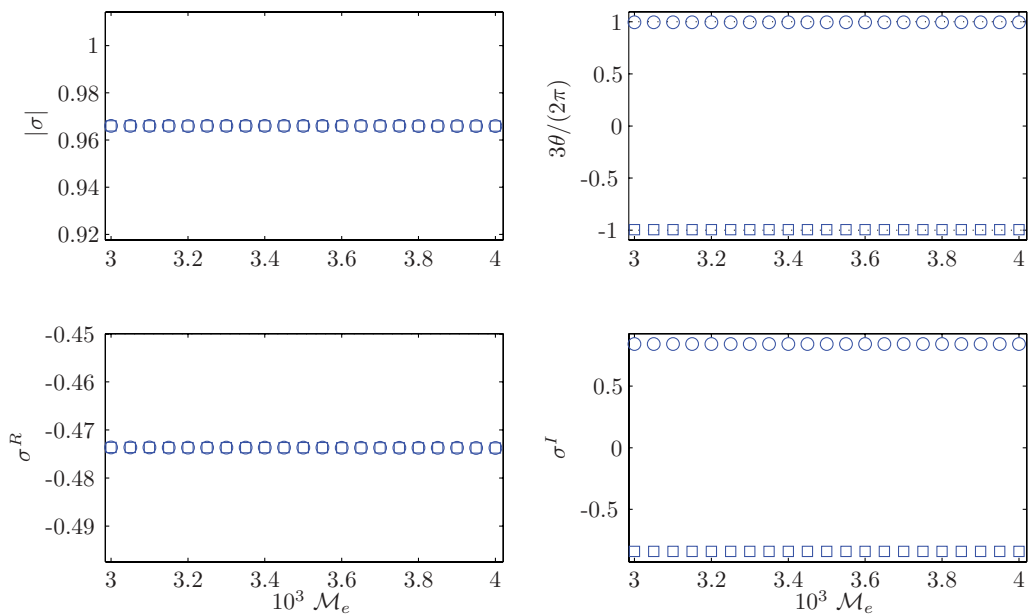


FIG. 7. (Color online) Floquet multipliers for stable T -periodic bubble oscillations away from wall ($S = 0$) at $\Omega = 0.0423$, indicating the presence of $3T$ -periodic oscillations. Circles and squares correspond to two distinct multipliers.

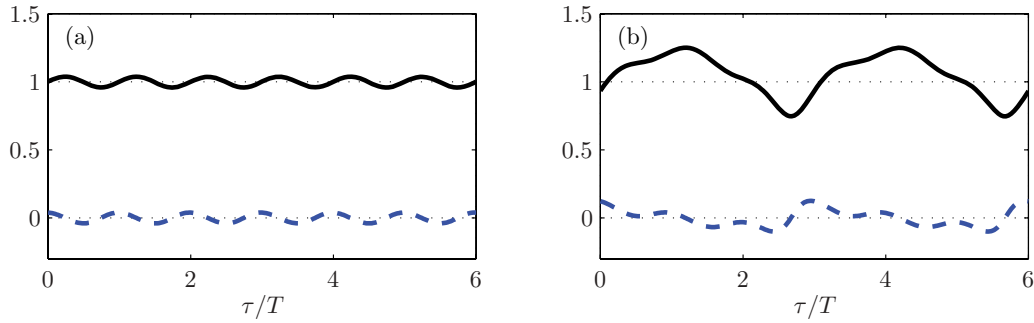


FIG. 8. (Color online) (a) Small and (b) large amplitude oscillations of bubble away from wall ($S = 0$) at $\Omega = 0.0423$ and $\mathcal{M}_e = 0.035$. The solid and dashed lines represent $r(\tau)$ and $\dot{r}(\tau)$, respectively.

presence of $4T$ -periodic solutions disjoint from the T -periodic oscillations. Such solutions were indeed found numerically; see Fig. 10(b). Thus we conclude that the period of large amplitude bubble oscillations depends on the proximity of the bubble to the wall and increases from $3T$ far away from the wall to $4T$ next to it. Floquet stability analysis (not detailed here) was performed for the $3T$ - and $4T$ -periodic large amplitude oscillations; in addition, equation (3) was solved numerically over several hundred forcing periods. This confirmed that the $3T$ - and $4T$ -periodic oscillations are stable and thus can coexist with small amplitude T -periodic oscillations.

Having established that the small and large amplitude oscillations illustrated in Figs. 8 and 10 cannot be obtained from each other by a parametric continuation, we ask a natural question: what defines the type of the observed oscillations in practice? Numerical experiments show that it depends not on the magnitude of the forcing, but rather on the initial conditions: large amplitude oscillations are typically established if a sufficiently large value of $\dot{r}(0)$ is specified. Physically, this corresponds to a pressure impulse that causes microbubbles to initially contract with a large speed and

then relax to large amplitude long-period oscillations. This is of particular practical significance since clinical ultrasound scanners do not apply continuous forcing, but employ a series of discrete pulses.

These numerical results emphasize that initial excitation can have a long-term (in fact, permanent and determining) effect on the observed bubble oscillation patterns. Therefore, the results of the analysis of the bubble dynamics based on numerically obtained bifurcation diagrams (Poincaré maps) that have been a popular tool of bubble dynamics analysis (see, e.g., [25,26,38]) have to be interpreted carefully. In obtaining such diagrams it is sometimes assumed that the initial conditions are “fully forgotten” once the transients have decayed and a periodic solution has been established. However, this might not be the case due to the existence of multiple solutions of a highly nonlinear system (3) each having its own basin of attraction [25]. Thus the initial conditions should be added to the set of parameters characterizing the solutions along with those given by (5). Failure to do so may lead to an ambiguous interpretation of the computed bubble dynamics.

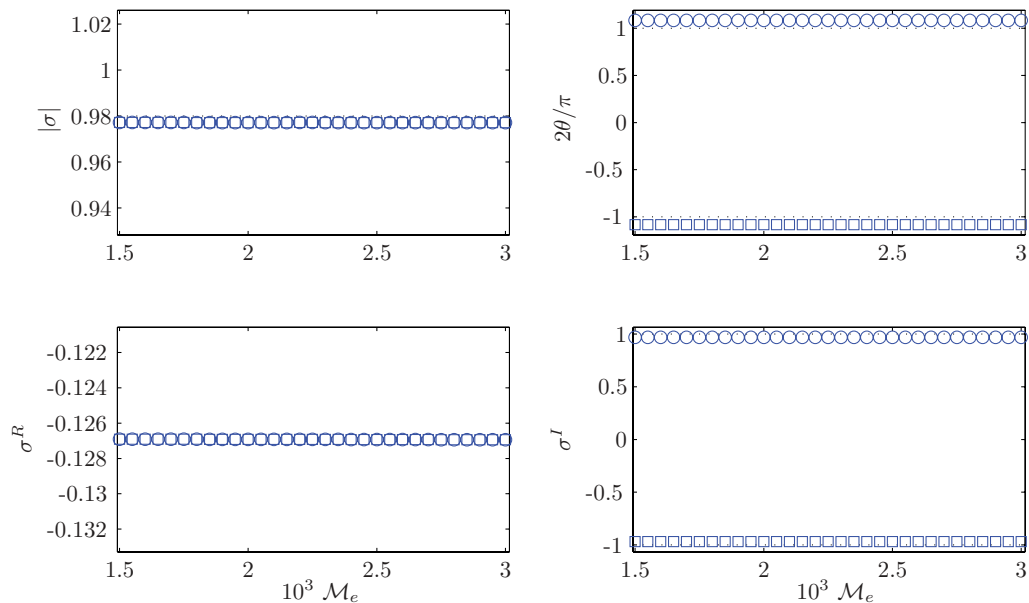


FIG. 9. (Color online) Floquet multipliers for stable T -periodic bubble oscillations of bubble near wall ($S = \frac{1}{2}$) at $\Omega = 0.0423$, indicating the presence of $4T$ -periodic oscillations. Circles and squares correspond to two distinct multipliers.

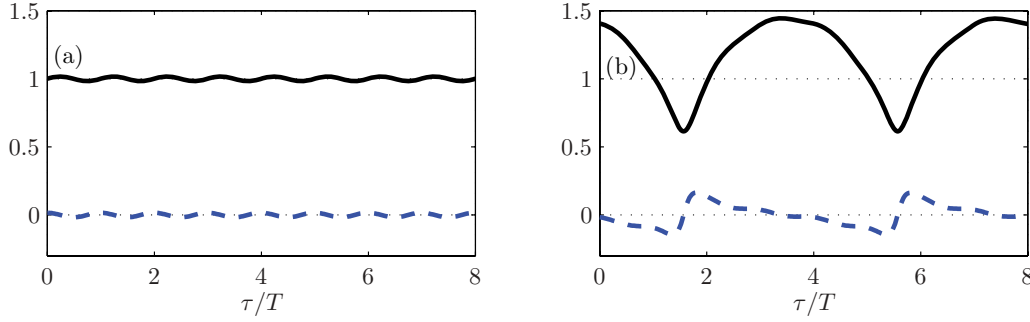


FIG. 10. (Color online) (a) Small and (b) large amplitude oscillations of bubble near wall ($S = \frac{1}{2}$) at $\Omega = 0.0423$ and $\mathcal{M}_e = 0.023$. The solid and dashed lines denote $r(\tau)$ and $\dot{r}(\tau)$, respectively.

VI. BUBBLE OSCILLATION MAPS

A. Bubble far from walls

Various types of oscillations that can be experienced by a microbubble located far away from a wall are summarized in Fig. 11. The line marked by circles is the parametric locus of a period-doubling bifurcation: T -periodic oscillations are stable below this line and stable $2T$ -periodic solutions replace them above it. The values of \mathcal{M}_e corresponding to the period-doubling bifurcation valid at least up to 4 significant digits were obtained iteratively by systematically applying the Floquet analysis implemented as described in the Appendix.

The $2T$ -periodic solution boundary has the characteristic minimum at $(\Omega, \mathcal{M}_e) \approx (0.029, 0.015)$ below which no bubbles can oscillate with the half-frequency of the driving ultrasound wave. Note that the above value of Ω virtually coincides with that at which the natural frequency ω_0 of small amplitude oscillations becomes equal to $\frac{1}{2}$ (see Fig. 3 and Table I). Therefore, the minimum driving pressure amplitude resulting in the transition to $2T$ -periodic solution occurs near the first subharmonic resonance observed in the system, an observation consistent with conclusions regarding the role of resonances in the bubble dynamics discussed in Ref. [25]. The existence of this minimum could also be qualitatively related to the amount of energy required to initiate and maintain

oscillations for various values of Ω . It is intuitively clear that the energy required to start oscillations (which is proportional to the square of the oscillation amplitude and thus to the square of the characteristic bubble radius) decreases with bubble size and so does $\mathcal{M}_{e,cr}$. However, as evidenced by Fig. 2 for small values of Ω , the value of \mathcal{M} (which is the parameter characterizing acoustic losses) increases rapidly, and so does the bubble energy loss rate [see the decrease in the relaxation time τ_0 in Fig. 3(a) that is inversely proportional to the energy loss rate]. To compensate for this enhancement of the oscillation energy loss due to acoustic radiation, the influx of the ultrasound energy has to increase in order to maintain oscillations. Thus the value of $\mathcal{M}_{e,cr}$ must increase for small bubbles. The minimum in the $\mathcal{M}_{e,cr}$ curve thus corresponds to the bubble size that ensures the minimum overall oscillation energy loss due to viscous dissipation and acoustic radiation.

Note that since $\Omega^2 \mathcal{M}_e = \frac{\alpha}{\rho c^2}$ we conclude that no bubble can produce a half-frequency response if

$$\alpha < \alpha_{2T} \approx 1.26 \times 10^{-5} \rho c^2 \approx 27.8 \text{ kPa.}$$

Therefore, setting $\alpha \approx \alpha_{2T}$ in an experiment and sweeping through a range of frequencies f_e , one can detect the value of frequency f_{2T} at which the half-frequency response is first heard. This would provide a straightforward estimation of the size of the bubble away from the wall

$$R_0 \sim 0.029 \frac{c}{2\pi f_{2T}} \approx \frac{6.9}{f_{2T}},$$

where f_{2T} is in MHz and R_0 is in μm . For example, for the considered frequency $f_e = 1$ MHz bubbles for which the half-frequency response would occur first would have the equilibrium radius $R_0 \approx 6.9 \mu\text{m}$.

The line marked by stars in Fig. 11 represents the minimum nondimensional amplitude of the ultrasound forcing at which stable large amplitude $3T$ -periodic oscillations were still detected numerically. These solutions, while remaining stable, cease to exist in a catastrophic way (resembling a fold bifurcation) when the value of \mathcal{M}_e is gradually decreased below the starred line. The smallest values of \mathcal{M}_e for which $3T$ -periodic solutions were still detected were determined up to 3 significant digits using the parametric continuation procedure detailed in the Appendix.

The resulting parametric boundary for the existence of $3T$ -periodic solutions has a minimum at $(\Omega, \mathcal{M}_e) \approx (0.040, 0.020)$. Again the parametric location of this minimum

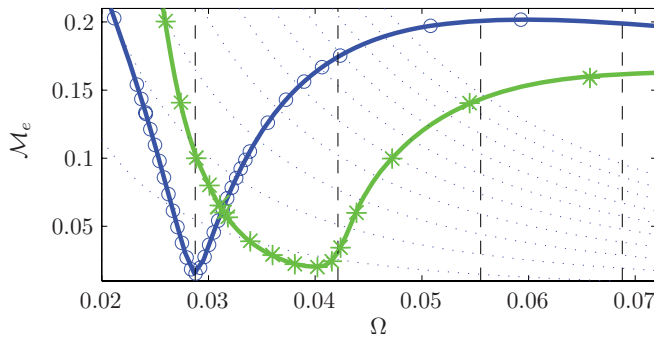


FIG. 11. (Color online) Oscillation map for a bubble away from wall ($S = 0$). The parametric boundaries for period-doubling and -tripling transitions are shown by circles and stars, respectively. Vertical dashed lines show the estimated positions of subharmonic resonances listed in the middle row of Table I. The dotted curves show isocontours $\alpha = \text{const.}$ with the values of α ranging (from left to right) from 100 to 1000 kPa at 100 kPa increments.

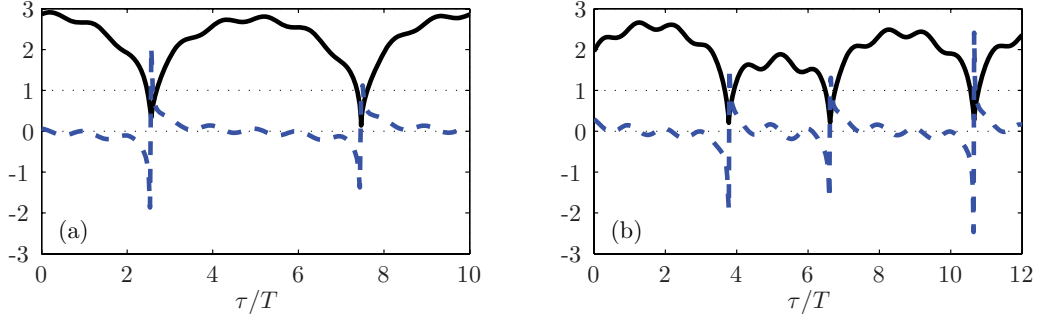


FIG. 12. (Color online) Combined bubble oscillations away from wall ($S = 0$) at $\Omega = 0.0423$ for (a) $\mathcal{M}_e = 0.18$ and (b) $\mathcal{M}_e = 0.25$. The solid and dashed lines represent $r(\tau)$ and $\dot{r}(\tau)$, respectively.

is close to the value of Ω where the bubble natural frequency ω_0 becomes equal to $\frac{1}{3}$ of the driving frequency, see Fig. 3(b), and thus it is closely linked to the occurring subharmonic resonance. A slight difference between the Ω location of the minimum and the resonance value reported in Table I is attributed to a nonlinear shift of the natural oscillation frequency occurring for finite amplitude oscillations. Based on the value of \mathcal{M}_e at the minimum we conclude that $3T$ -periodic oscillations can only be maintained for

$$\alpha > \alpha_{3T} \approx 3.2 \times 10^{-5} \rho c^2 \approx 70.5 \text{ kPa},$$

and the bubble size estimation formula based on the period-tripling frequency f_{3T} becomes

$$R_0 \sim 0.040 \frac{c}{2\pi f_{3T}} \approx \frac{9.5}{f_{3T}},$$

where f_{3T} is in MHz and R_0 is in μm . However, given that $3T$ -periodic solutions usually require an initial pressure pulse to induce, using this correlation in practical experiments may be less convenient than that for $2T$ -periodic oscillations. The $2T$ - and $3T$ -periodic solution boundaries intersect at $(\Omega, \mathcal{M}_e) \approx (0.0313, 0.0626)$. Therefore, it is expected that as the driving pressure amplitude increases the oscillations of smaller bubbles to the left of the intersection point will always experience period-doubling before $3T$ -periodic oscillations can be observed. This fact was also illustrated by Figs. 10(a) and 12(a) in Ref. [26]. The situation is much more complicated for larger bubbles. For small forcing amplitudes, in the region

below the line marked by stars in Fig. 11, only small amplitude T -periodic oscillations can be observed. In the region between the lines marked by stars and circles, both stable T and $3T$ periodic oscillations can exist, and the type of oscillations established is determined by the initial conditions. Above the curve marked by circles, T -periodic solutions become unstable and cannot be observed. They are replaced by stable $2T$ -periodic oscillations; see Fig. 5. Again, depending on the initial conditions the $3T$ -periodic solutions also can exist in this region as was observed in our numerical computations just above the $2T$ transition boundary. However, for larger values of \mathcal{M}_e , combination solutions involving both $3T$ and $2T$ components are also observed. In some instances such solutions appear as $5T$ -periodic oscillations; see Fig. 12(a). Note that the physical parameters for which this plot is generated are identical to those chosen for Fig. 5(b), yet the long-term solutions obtained for different initial conditions differ drastically. In other cases the strongly nonlinear interaction between these large amplitude solutions leads to what appears to be aperiodic oscillations [see Fig. 12(b)], frequently referred to as chaotic behavior in literature. Thus we can state that the parametric region above both curves in Fig. 11 is where chaotic bubble oscillations can potentially be observed. This region protrudes toward smaller forcing amplitudes near the intersection of the two curves. Therefore, the curve intersection point defines the size of the bubbles that are most likely to enter the chaotic regime away from the wall. For $f_e = 1$ MHz it is $R_0 \approx 7.4 \mu\text{m}$.

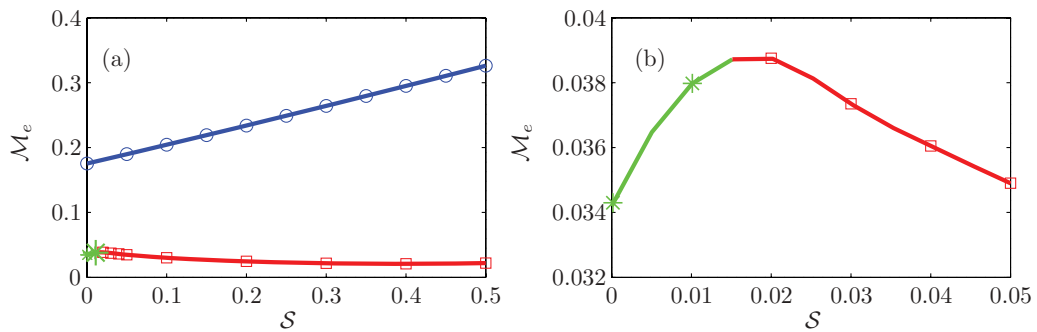


FIG. 13. (Color online) Oscillation map for bubble approaching wall for $\Omega = 0.0423$: (a) complete diagram, (b) close up for distant bubbles (computational points are shown by symbols, the lines represent a spline interpolation of the data). The parametric boundaries for period-doubling, -tripling, and -quadrupling transitions are shown by circles, stars, and squares, respectively.

The higher order subharmonic resonances that are expected to exist for a bubble away from the wall near other vertical dashed lines in Fig. 11 did not seem to lead to the appearance of nT -periodic ($n > 3$) oscillations at least for the range of parameters in the figure. We chose not to look for such solutions at larger values of \mathcal{M}_e , since they would be far outside the practical range of ultrasound amplitudes that corresponds to the region between dotted curves in Fig. 11.

B. Bubble close to a wall

To investigate the effect of the wall proximity on bubble dynamics, we consider an oscillation map produced for $\Omega = 0.0423$ (corresponding to $R_0 = 10 \mu\text{m}$), with \mathcal{S} varying from 0 (bubble away from the wall) to $\frac{1}{2}$ (bubble near the wall). The results are presented in Fig. 13. The only effect the wall proximity has on the bubble’s tendency to undergo a period-doubling bifurcation is quantitative: an essentially linear increase of the critical value of \mathcal{M}_e approximately given by

$$\mathcal{M}_{e_{cr}} = \mathcal{M}_{e_{cr0}} + d\mathcal{S}.$$

For $\Omega = 0.0423$ and other parameters corresponding to this value ($\mathcal{R} = 6.4 \times 10^{-3}$, $\mathcal{W} = 3.7 \times 10^{-3}$, $\mathcal{M} = 2.47 \times 10^{-2}$; see Fig. 2) $\mathcal{M}_{e_{cr0}} \approx 0.0175$ and $d \approx 0.3$. It was noted in the comparison of Figs. 5 and 6 that the presence of the wall can delay the transition to a doubly periodic regime by a factor of almost two in forcing amplitude. This is intuitively expected as the wall is modelled by introducing an identical bubble image so that when the bubble approaches the wall the external ultrasound radiation effectively has to drive two bubbles instead of one.

In contrast to small amplitude solutions, strongly nonlinear large amplitude oscillations undergo a qualitative change in the vicinity of the wall: the period of such oscillations changes from $3T$ away from the wall to $4T$ when the bubble approaches the wall; see lines marked by stars and squares in Fig. 13. Such a switch occurs between $\mathcal{S} = 0.01$ and $\mathcal{S} = 0.02$ [see Fig. 13(b)]; that is, when the bubble is between 25 and 50 radial distances away from the wall. Therefore, the influence of the wall on the large amplitude oscillations is far reaching. Another important observation is that the forcing amplitude \mathcal{M}_e decreases along the boundary of $4T$ -periodic oscillations as the bubble approaches the wall. Therefore, it becomes easier to induce such oscillations near the wall. Both these facts suggest that the appearance of the quarter frequencies in the bubble acoustic response spectra can be used in practice as an indication of the bubble’s approach to the wall. In Fig. 14 we present the parametric boundaries for transitions to various long-period oscillations of a near-wall bubble. The comparison with Fig. 11 shows that the proximity of the wall leads to significantly more complicated bubble dynamics characterized by the appearance of different oscillation modes that depend sensitively on the nondimensional bubble radius Ω . The shape of the parametric line showing the locations of period-doubling bifurcations remains similar to that seen in Fig. 11 for a bubble away from the wall, with the minimum detected at the first subharmonic resonance (see the bottom row in Table I). However, the figure shows that

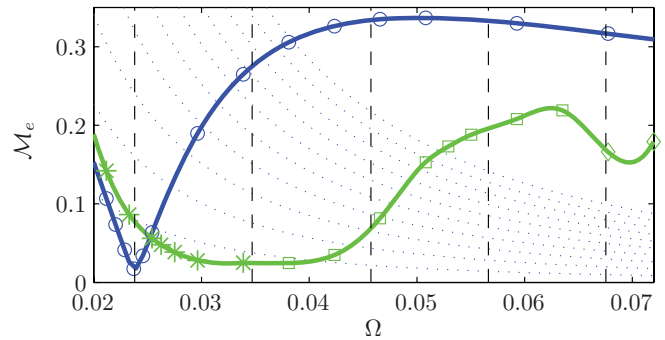


FIG. 14. (Color online) Oscillation map for bubble near wall ($\mathcal{S} = \frac{1}{2}$). The parametric boundaries for transitions to $2T$ -, $3T$ -, $4T$ -, and $5T$ -periodic oscillations are shown by circles, stars, squares, and diamonds, respectively. Vertical dashed lines show the estimated positions of subharmonic resonances listed in the bottom row in Table I. The dotted curves show isocontours $\alpha = \text{const}$ with the values of α ranging (from left to right) from 100 to 1000 kPa at 100 kPa increments.

the behavior of bubbles of different sizes as they approach the wall is not the same. Namely, the excitation amplitude at which the period doubling is observed for bubbles with a nondimensional radius $\Omega \lesssim 0.026$ ($R_0 \lesssim 6 \mu\text{m}$) is decreasing as they approach the wall, while for larger bubbles it increases. A similar conclusion follows from comparing Figs. 11 and 14 regarding the long-period oscillations; however, with one drastic difference: Near-wall bubbles tend to oscillate with various frequencies that depend on their size: the larger the size of a bubble, the longer period of oscillations it has. For example, $3T$ -periodic oscillations are most profound near the second subharmonic resonance (stars in Fig. 14). They are replaced with $4T$ - (squares) and $5T$ - (diamonds) periodic oscillations as Ω increases, but such long-period oscillations are not expected to be seen for forcing amplitudes commonly used in medical practice. As noted earlier, the tendency of a near-wall bubble to undergo longer period oscillations is apparently linked to the presence of a bubble image in the model that effectively increases the bubble inertia; note that the \mathcal{S} term plays the role of an additional mass in the left-hand side of equation (3).

It is also instructive to note that irregular oscillations can be observed at values of \mathcal{M}_e smaller than those shown by squares and diamonds in Fig. 14 for some initial conditions. They could be mistaken for “chaotic bubble behaviour.” In reality they appear to be just transient solutions that eventually settle to simple T -periodic oscillations. However, this may take a very long time (e.g., up to 20 000 forcing periods in our computations). The fact that they eventually decay while regular multiperiod oscillations persist confirms once again that the appearance of the latter is due to subharmonic resonances which facilitate absorption of ultrasound energy by the resonating bubbles.

VII. CONCLUSIONS

The behavior of a microbubble approaching a solid wall and subjected to ultrasound forcing has been investigated using a modified Keller-Miksis-Parlitz equation [25,32] as a

base model. Floquet analysis has been applied to investigate the stability of the small amplitude solutions and predicts the regions of existence of various fully nonlinear large amplitude oscillations. It has been shown that microbubble response to acoustic forcing can consist of T -, $2T$ -, and $3T$ -periodic oscillations (T is the period of ultrasound forcing) when the bubble is away from the wall and T -, $2T$ -, $4T$ -, and $5T$ -periodic oscillations when the bubble is near it. We also showed that a bubble starts “feeling” the presence of the wall and changes its acoustic response when it is as far from the wall as 25–50 radial distances away. It is found that, in all cases, $2T$ oscillations appear as a result of supercritical period-doubling bifurcations of T -periodic solutions, while longer periodic oscillations are completely disjoint from the T - and $2T$ -periodic solutions and usually require a pressure impulse to be initiated.

Although several physical details were neglected for simplicity, such as the presence of a shell encapsulating medical microbubbles, the Bjerknes force that could cause a bubble on a wall to deform, and compliance of the wall material, the existence of clear differences in the dynamical-systems behavior owing to the presence of a wall suggests that more detailed studies are warranted. The results of future investigations could be used to estimate both the size of the bubble and its proximity to the wall based on the spectrum of the bubble’s acoustic signature.

The demonstrated existence of multiple oscillatory solutions also strongly indicates that bifurcation diagrams (Poincaré maps) that are frequently used in studies of bubble dynamics could be misleading unless initial conditions used to obtain such diagrams are clearly stated and added to the set of the governing parameters characterizing the problem.

APPENDIX: NUMERICAL ASPECTS

The major value of Floquet analysis is its ability to predict very accurately various period-changing bifurcations. However, this requires the explicit knowledge of the periodic solution $(r_0(\tau), \dot{r}_0(\tau))$ stability of which it aims to investigate. One may try to use a “brutal force” approach by integrating the governing equation (3) starting with some arbitrary initial conditions over a sufficiently long time to allow all transients to decay and a periodic (limit cycle) solution to establish. However, this can only work if this solution is stable.

Yet to determine the bifurcation point iteratively one needs to compute Floquet multipliers and thus know the periodic solution $(r_0(\tau), \dot{r}_0(\tau))$ in parametric regions where this solution becomes unstable and thus cannot be obtained using forward time integration. Therefore, instead of solving (3) as an initial value problem one needs to view it as a periodic boundary problem with a specified period (the forcing period or its integer multiple). Solving such a boundary value problem is done iteratively and the convergence of iterations depends sensitively on the initial guess. For T -periodic oscillations it is readily available from a large time limit of Eq. (8) and the iterative determination of one period-doubling bifurcation point takes just a few seconds of CPU time.

However, this analytic solution cannot be used as an initial guess for large amplitude long period oscillations. In fact, it is not even known whether such solutions exist as they are fully disjoint from the T - and $2T$ -periodic solutions naturally linked to (8). Therefore, first we used the analysis of the phase θ of Floquet multipliers (see Figs. 7 and 9) of the T -periodic solutions to establish parametric ranges where fully nonlinear large amplitude long period solutions can possibly exist. Then for a so-selected set of governing parameters we tested a number of empirically chosen “pressure impulse” initial conditions to obtain a stable large amplitude solution using forward time integration. Numerically, this was done by specifying a sufficiently large (typically of order 10^{-1} or even 1) negative value of \dot{r}_0 .

Once the first long term nT -periodic ($n > 2$) solution was obtained in such a way, similarly to (8) offering a suitable initial guess for solving a periodic boundary value problem for small amplitude solutions, it can be used as a natural initial guess for a periodic boundary value problem for large amplitude oscillations. However, we found that solving it for nT -periodic oscillations still encountered significant numerical difficulties due to the cusp-like singularity developing near the minima of the bubble contraction curves (see Fig. 12). This singularity frequently results in the divergence of iterations due to the local loss of numerical approximation near the cusp. Since the location of such a cusp changes during iterations, adaptively increasing the local grid density near it to recover the approximation accuracy becomes a technical challenge. For this reason in the current study we chose not to solve a periodic boundary value problem for long period nonlinear oscillations. Instead we used a more robust forward time integration; for example, implemented in MATLAB’s function `ode15s` for numerically stiff problems for all large amplitude oscillations since it has a built-in automatic algorithm for reducing a computational step when the time derivative becomes large.

As discussed above, only stable oscillations can be obtained using this approach so that an automatic iterative search of the transition point based on Floquet multipliers that was successfully implemented for small amplitude oscillations cannot be guaranteed to work for large amplitude nT -periodic solutions. Therefore, instead, once the first of such solutions was obtained as discussed above, the governing physical parameters were gradually changed and the final values of (r_0, \dot{r}_0) from a previous forward time integration run were used as initial values for a new run in order to trace the variation of large amplitude solutions with \mathcal{M}_e , \mathcal{S} and Ω . The length of each such run was between 900 and 4000 forcing periods (between 50 and 300 relaxation time units τ_0) to allow for statistically steady oscillations to establish. The longest runs took up to 4 min on a standard desktop computer.

The lines representing nT -periodic solutions in Figs. 11, 13, and 14 were obtained in this way and thus they correspond to parametric values at which the respective long period numerical solutions cannot be found any more by forward time integration using the above parametric continuation procedure toward smaller values of \mathcal{M}_e .

- [1] N. de Jong, A. Bouakaz, and P. Frinking, *Echocardiogr.-J. Card.* **19**, 229 (2002).
- [2] C. E. Brennen, *J. Fluid Mech.* **472**, 153 (2002).
- [3] J. R. Lindner, *Nat. Rev. Drug Discovery* **3**, 527 (2004).
- [4] M. W. Grinstaff and K. S. Suslick, *Proc. Nat. Acad. Sci. USA* **88**, 7708 (1991).
- [5] E. Stride and M. Edirisinghe, *Soft Matter* **4**, 2350 (2008).
- [6] M. Postema and G. Schmitz, *Ultrason. Sonochem.* **14**, 438 (2007).
- [7] A. L. Klibanov, *Med. Biol. Eng. Comput.* **47**, 875 (2009).
- [8] A. A. Doinikov, S. Zhao, and P. A. Dayton, *Ultrasonics* **49**, 195 (2009).
- [9] S. Qin, C. F. Caskey, and K. W. Ferrara, *Phys. Med. Biol.* **54**, R27 (2009).
- [10] J. R. Lindner, *Cardiovasc. Res.* **84**, 182 (2009).
- [11] S. Zhao, D. E. Kruse, K. W. Ferrara, and P. A. Dayton, *J. Acoust. Soc. Am.* **120**, EL63 (2006).
- [12] A. V. Patil, J. J. Rychak, J. S. Allen, A. L. Klibanov, and J. A. Hossack, *Ultrasound Med. Biol.* **35**, 2021 (2009).
- [13] A. V. Patil, J. J. Rychak, A. L. Klibanov, and J. A. Hossack, *Mol. Imaging* **10**, 238 (2011).
- [14] S. Zhao, D. E. Kruse, K. W. Ferrara, and P. A. Dayton, *Phys. Med. Biol.* **52**, 2055 (2007).
- [15] E. Payne, A. Ooi, and R. Manasseh, *Ther. Delivery* **2**, 213 (2011).
- [16] R. Manasseh and A. Ooi, *Bubble Sci., Eng., and Technol.* **1**, 58 (2009).
- [17] M. Strasberg, *J. Acoust. Soc. Am.* **25**, 536 (1953).
- [18] E. M. B. Payne, S. J. Illesinghe, A. Ooi, and R. Manasseh, *J. Acoust. Soc. Am.* **118**, 2841 (2005).
- [19] M. Overvelde, V. Garbin, B. Dollet, N. de Jong, D. Lohse, and M. Versluis, *Ultrasound Med. Biol.* **37**, 1500 (2011).
- [20] B. Dollet, W. van Hoeve, J.-P. Raven, P. Marmottant, and M. Versluis, *Phys. Rev. Lett.* **100** 034504 (2008).
- [21] C. Chen, Y. Zhu, P. W. Leech, and R. Manasseh, *Applied Phys. Lett.* **95**, 144101 (2009).
- [22] T. G. Leighton, D. G. Ramble, A. D. Phelps, C. L. Morfey, and P. P. Harris, *Acustica:Acta Acustica* **84**, 801 (1998).
- [23] T. G. Leighton, K. Baik, and J. Jiang, *Proc. R. Soc. A* **1** (2012).
- [24] W. Lauterborn, *J. Acoust. Soc. Am.* **59**, 283 (1976).
- [25] U. Parlitz, V. Englisch, C. Scheffczyk, and W. Lauterborn, *J. Acoust. Soc. Am.* **88**, 1061 (1990).
- [26] K. J. Y. Chong, C. Y. Quek, F. Dzaharudin, A. Ooi, and R. Manasseh, *J. Sound Vib.* **329**, 687 (2010).
- [27] R. Mettin, I. Akhatov, U. Parlitz, C. D. Ohl, and W. Lauterborn, *Phys. Rev. E* **56**, 2924 (1997).
- [28] H. J. Vos, B. Dollet, J. G. Bosch, M. Versluis, and N. de Jong, *Ultrasound Med. Bio.* **34**, 685 (2008).
- [29] J. S. Allen, D. J. May, and K. W. Ferrara, *Ultrasound Med. Biol.* **28**, 805 (2002).
- [30] S. Paul, A. Katiyar, K. Sarkar, D. Chatterjee, W. T. Shi, and F. Forsberg, *J. Acoust. Soc. Am.* **127**, 3846 (2010).
- [31] A. A. Doinikov, L. Aired, and A. Bouakaz, *Phys. Med. Biol.* **56**, 6951 (2011).
- [32] J. B. Keller and M. Miksis, *J. Acoust. Soc. Am.* **68**, 628 (1980).
- [33] A. Shima and Y. Tomita, *Archive Appl. Mech.* **51**, 243 (1981).
- [34] T. G. Leighton, *The Acoustic Bubble* (Academic Press, San Diego, California, USA, 1994).
- [35] M. Li, F. Dzaharudin, A. Ooi, and R. Manasseh, in *Proceedings of 20th International Congress on Acoustics, ICA 2010* (Australian Acoustical Society, Sydney, 2010), p. 369.
- [36] S. J. Illesinghe, A. Ooi, and R. Manasseh, *J. Acoust. Soc. Am.* **126**, 2929 (2009).
- [37] A. H. Nayfeh and B. Balachandran, *Applied Nonlinear Dynamics, Analytical, Computational and Experimental Methods*, Wiley Series in Nonlinear Science (John Wiley and Sons, New York, 1995).
- [38] C. A. Macdonald and J. Gomatam, *Proc. Inst. Mech. Eng., Part C* **220**, 333 (2006).